J Mater Sci (2011) 46:4494–4508
DOI 10.1007/s10853-011-5343-9

# Fracture features in soda-lime glass after testing with a spherical indenter

**Andreas Momber**

Received: 12 September 2010 / Accepted: 27 January 2011 / Published online: 15 February 2011


**Abstract** A thick soda-lime glass plate was indented with a spherical indenter at high indentation forces up to 1.839 kN. A systematisation of the fracture figures showed a basic structure, consisting of four individual zones. The detailed characteristics of these zones depended on indentation force. Existing models for the assessment of contact diameter and radial and lateral vent cracks length were proven. The appearance of fracture lances was observed and discussed. It was found that these lances formed during the intersection of conchoidal (lateral) fractures, and that their formation was bound to the elastic-plastic period of the indentation process. Features of fracture lances, namely the formation of numerous symmetric lance fronts, periodically occurring lance fronts, lance front statistics, and lance dimensions were described and discussed in detail. It was also shown that the formation of fracture lances showed elements of self-similarity and fractal geometry.

## Introduction

Studies of how materials fail are crucial to the ability to design and engineer better materials, for example, to create lighter, stronger, or tougher materials. Situations where two materials are in small-scale contact belong to the most common loading situations in engineering. Cracking processes occurring in materials during indentation with spherical indenters are of special complexity. Cracks subjected to mixed loading conditions display a particularly intriguing behavior. It was suggested recently to design material structures that induce local combined tension-tear loading to increase a structure's resistance to failure [1]. From that point of view, the formation of fracture lances, as a result of mixed loading, will require particular attention, namely for small-scale contact conditions.

Systematic investigations into the indentation of glass by spherical indenters were first performed by Auerbach [2]. Classical crack types formed due to elastic material response during the contact between glass samples and spherical indenters are ring cracks and cone cracks. However, no notice is often taken of radial vent cracks and lateral vent cracks, which can form during the indentation with rather blunt indenters at high forces due to elastic-plastic material response. Investigations of Peter [3] have notably contributed to the understanding of the response of soda-lime glass to indentation. He could show that small curvature radii promoted elastic-plastic response and that cracks formed perpendicular to the surface after unloading. Peter defined three critical ranges for the indenter curvature, where glass responded either elastic or elastic-plastic. The lower radius of curvature, where Hertzian cone cracks reliably formed, was about 135 μm. Swain and Hagan [4] performed a systematic study of spherical indentations on various glasses, and they have shown that for small indenters (<1,000 μm) plastic flow as well as Hertzian cone cracking occurred. They also noted and described a series of radial vent cracks on unloading and an independent system of lateral vent cracks just before complete unloading. Indentation forces applied in their study were between 0.02 and 0.5 kN, while the diameters of the indenters varied between 0.4 and 1.0 mm. Persson et al. [5] investigated the response of soda-lime glass to rather large (3 mm) steel indenters. At low forces (up to 0.2 kN), ring cracks started to form. At forces between 0.4 and 0.5 kN,

A. Momber (✉)
Faculty of Georesources and Materials Engineering,
Rheinisch-Westfälische Technische Hochschule Aachen,
Brunsstraße 10, 21073 Hamburg, Germany
e-mail: andreas.momber@t-online.de

more than one ring crack was present. Between force levels of 0.5 and 1.0 kN, lateral vent crack formed and propagated almost parallel to the surface. In a few cases, at forces of 0.8 kN, radial vent cracks were identified. At extremely high loads in excess of 2.5 kN material right below the indenter had been crushed. However, the authors did not provide a detailed fractographic analysis. Gorham and co-workers [6–8] offered a systematization of damage features observed during the indentation of soda-lime glass with large spherical indenters (diameter 5 mm) at indentation forces between 0.2 and 1.5 kN. Based on the observed crack and fracture features and in dependence of the applied forces, the fracture events were categorized into seven ranges. Ranges with low indentation forces (0.3–0.6 kN) were characterized by elastic response and Hertzian cone cracks formed. At higher forces (up to 2.0 kN), phenomena could be observed which were typical for rather "sharp" indenter shapes. These included elastic-plastic material response, namely densification, plastic flow, localized crushing during the loading period, and the formation of radial and lateral vent cracks during the unloading period. The studies performed in this article refer to these investigations in order to discuss the fracture features in more detail and to discuss additional features not reported in the above mentioned references.

The analysis of the fracture plane morphology helps to gather more information on the processes of fracture initiation and fracture progression. During the progression of fractures in glass, a three-zone fracture figure can generally be observed [9, 10]. This fracture zone subdivision was frequently applied to interpretations of indentation tests at brittle materials. The reader may refer to the works of [11–13]. A detailed electron microscope study on the microcracking features about indentations in ceramics caused by Vickers indenters was performed in [14]. A very particular result of that investigation was the detection of distinguished fracture marks on the surface of lateral fractures. The authors noted that cracks broke up into partial fronts and contributed this effect to some shear disturbances. Such fracture marks, formed after the indentation of soda-lime glass with a nano-indenter, can also be detected on photographs published in [15], whereat these authors did not spend attention to the marks. A survey on papers on glass testing revealed that this particular behavior, which will be discussed in detail in due of this article, occurred under very different loading situations. A summary is provided in Table 1. Crack front segmentation, or fracture lance formation, seems to be a fundamental process closely related to glass failure. In spite of the general advantage of local mixed-mode loading to the resistance of materials to failure [1], a closer look at this phenomenon under contact conditions can notably contribute not only to a better understanding of indentation-based material testing, but also to the design of "indentation resistant" materials.

## Target material and experimental set-up

All indentation experiments were performed with a conventional Rockwell hardness tester, type *Wolpert HAT1a/HAT2a* with indentation forces between 0.15 and 1.84 kN. The contact period was 25 s for each test. The indenter was a standard tungsten carbide sphere with a diameter of 1.0 mm. Five indentation tests were performed for each test configuration. The material tested was a commercial soda-lime glass plate with a thickness of 30 mm. The element composition of the glass was estimated with EDX analysis. The corresponding EDX diagram is shown in Fig. 1. The glass contained calcium and soda as network formers. The indented sites were inspected, after the loading process was completed, under a high-resolution

**Table 1** Detection of crack front segmentation (fracture lance formation) in papers on glass testing

| Test condition/sample | Glass type | References |
|---|---|---|
| Nano-indentation of glass sheets | Soda-lime glass | [15] |
| Heating/cooling of small containers | Sheet glass | [16] |
| Tensile test with imposed internal pressure on bars | Soda-lime glass | [17] |
| | Boron-silica glass | |
| Tensile test with imposed internal pressure on bars | Quartz glass | [18] |
| Tensile test with imposed internal pressure on bars | AR glass | [19] |
| Modified compact tension specimen | Soda-lime glass | [20] |
| Impact on confined bars | Soda-lime glass | [21] |
| Low-speed steel ball impact | Soda-lime glass | [22] |
| Three-point bend test | Soda-lime glass | [23] |
| Cyclic bending (fatigue) | Engineering glass | [24] |
| Axial splitting (compressive) of cylinder samples | Soda-lime glass | [25] |
| Solid particle impingement of glass plates | Soda-lime glass | [26] |

Results of a survey performed by the author

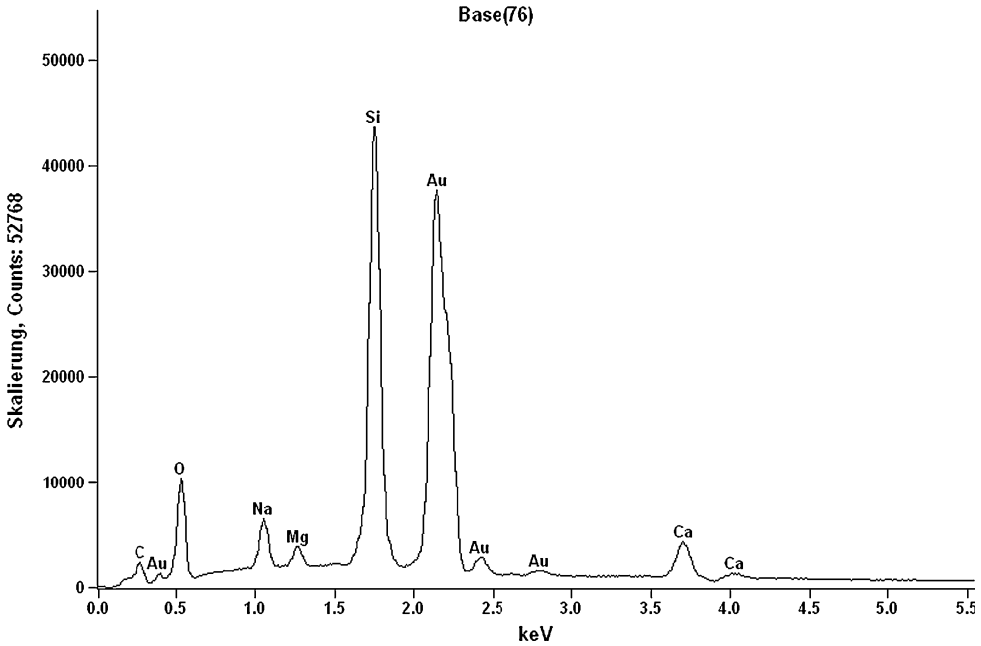


**Fig. 1** Element composition of the used glass sample (EDX spectrum)

optical microscope, partially under incident light. All crack dimensions reported in this article were carefully measured under the microscope with a high accuracy using different standard scales.

## Description of fracture morphology

### Moderate indentation forces

The results of the fracture surface inspections indicated a rather complex structure of the fracture features, similar to those reported in [3–5, 7, 8, 27]. Examples of fracture morphologies, which summarize many of the observed phenomena, are shown in Fig. 2 for two different force levels. The respective phenomena are schematically illustrated in the right section of either figure.

The situation for a moderate force is displayed in Fig. 2a. The central range *1*, denoted *center* in this article, was virtually the contact area between indenter and target surface. During loading, compressive stresses were generated in this range. This range was not affected in Fig. 2a; it was neither deformed nor was the surface broken. This unaffected state, however, could be maintained under certain conditions only. The relationship between indentation force and the center diameter is graphically illustrated in Fig. 3. It can be seen that the diameter increased if the force increased, in which the relationship between indentation force and center diameter became less relevant at high forces. This latter tendency was also reported in [28] in the result of quasi-static indentation tests. In the range of the open symbols plotted in Fig. 3, micro cracks could be observed, and the border of the center could not be identified precisely. The center was surrounded by a ring section, which is denoted *2* in Fig. 2a. It was characterized by microscopically small debris in the glass surface, similar to observations reported in [29]. The ring section disappeared at high indentation forces. The range *3* in Fig. 2a was characterized by the formation of radial vent cracks whose origination during spherical indentation was in detail discussed in [4, 30]. In Fig. 2a, the radial vent cracks propagating underneath the sample surface could be recognized as small dark wedges. Results of radial vent crack measurements are plotted in Fig. 4 in a way suggested in [30]. It can be seen that the lengths of the radial vent cracks increased with an increase in indentation force. The ring *4*, a ring crack, formed the outer border of the crack, or fracture, figure in radial direction. The diameter of these rings ($D_2$) depended on the indentation forces. Results of measurements are provided in Fig. 5. In tendency, the diameter increased with an increase in indentation force, whereas the values for the lower forces did not fit into the suggested relationship.

### High indentation forces

The situation for a rather high force is pictured in Fig. 2b. The gray central region, denoted *5* in the diagram, was an irreversibly deformed surface region. This center region was considered to be the contact area in the elastic-plastic response regime. Results of measurements of this region are presented in Fig. 3. The regions *3* and *9* were characterized by dominant lateral fractures, separated by radial vent cracks (*8*). An outer curved crack, denoted *7* in the

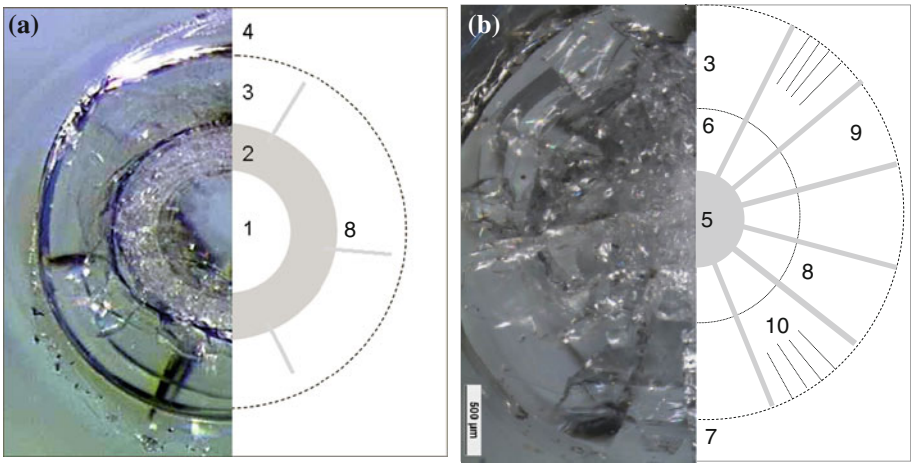


**Fig. 2** Typical fracture morphologies of loaded samples. Microscopy image (light microscope) (*left*) and schematic illustration (*right*). **a** Moderate indentation force. **b** High indentation force. *1*/*5* center, *2*/*6* micro fracture ring, *3* crack/fracture zone, *4*/*7* outer ring, *8* radial vent cracks, *9* lateral fractures, *10* fracture lance front

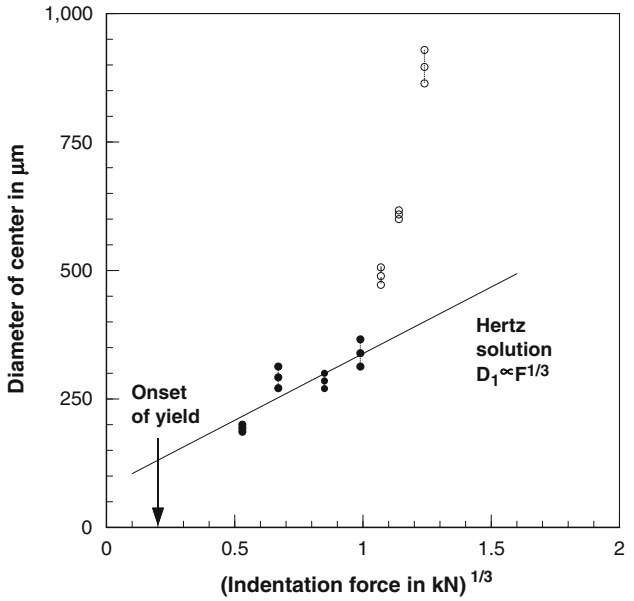


**Fig. 3** Relationship between indentation force and center diameter. *Open symbols* characterize situations with notable micro fracture formation, *solid line* represents Eq. 5

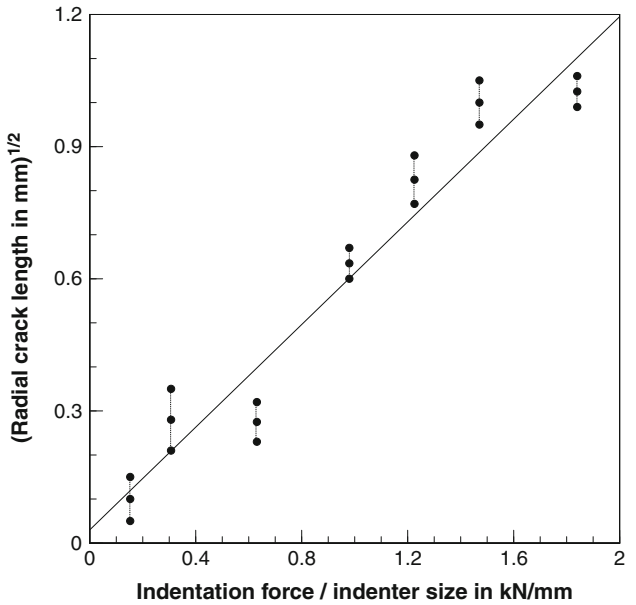


**Fig. 4** Relationship between indentation force and radial vent crack length. *Solid line* represents Eq. 6

diagram, could be recognized, which bordered the crack figure in radial direction. Results of measurements of these rings are provided in Fig. 5. In tendency, the diameter increased with an increase in indentation force. The notation *9* characterized regions with notable lateral conchoidal fractures, separated through lateral vent cracks (*8*). In this region, fracture lances (*10*), which will be reported about in detail in a following section, appeared frequently.

## Generalization of indentation force effects

Effects of the indentation forces on the precise structure of the crack, or fracture, morphologies are generalized in Table 2 based on microscope images. The different magnification grades of the photographs must be considered. At low force ($F = 0.153$ kN), the center remained unaffected, but it was surrounded by a ring consisting of slightly damaged surface segments. Lateral vent cracks could not be identified clearly, while radial vent cracks could. An increase in force to $F = 0.307$ kN led to the formation of considerable radial vent cracks. The inner ring was surrounded by slight conchoidal fractures. The surfaces of these regions (left image section) showed traces of fracture lances. The images for $F = 0.613$ kN delivered very similar findings. However, radial vent cracks were less pronounced. At $F = 0.981$ kN, the center was still unaffected, but the inner ring section, consisting of damaged surface

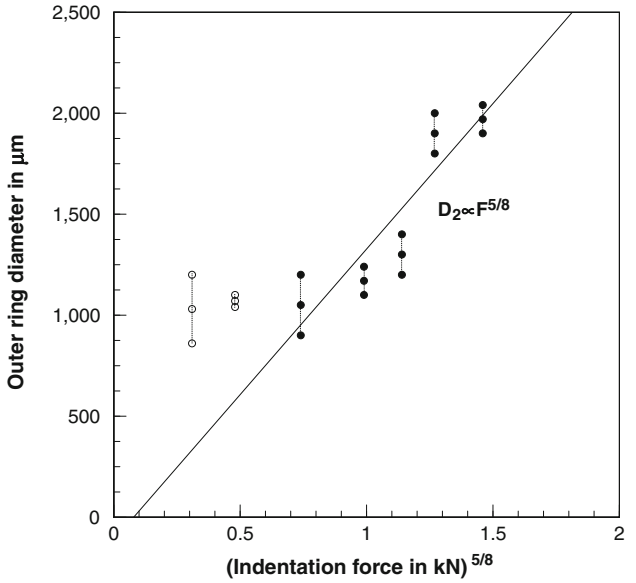


**Fig. 5** Relationship between indentation force and outer ring diameter. *Filled symbols* characterize situations with notable micro fracture formation, *solid line* represents Eq. 1

segments, was well defined. At the outer end of that ring, localized conchoidal fractures could be noted. Radial vent cracks were clearly in evidence. The outer ring was very pronounced; it also featured fracture lances at its internal surface. As the force increased further up to $F = 1.226$ kN, the fracture appearance notably changed. The center was irreversibly deformed. Glass debris was broken off the surface, and the center was partially crushed. The inner ring section was not clearly distinguishable anymore. It passed on into a range of large lateral conchoidal fractures, separated through radial vent cracks. This range extended up to the outer ring, which was also not clearly distinguishable. Lateral conchoidal fractures formed (lower section of the photograph). Discrete small debris could be recognized in the lower left region of the image. The formation of radial vent cracks became evident. The situation for $F = 1.471$ kN was characterized by an extensive destruction of the center. Glass segments seemed to be separated by radial vent cracks. These separated segments were additionally separated in radial direction by means of fractures. These fractures were located at about half of the lengths of the segments. The shapes of these segments agreed with fragments observed in [8] during indentation tests on glass. The inner ring section disappeared completely. Conchoidal fractures started immediately at the perimeter of the center zone and they extended up to the outer ring, which was not clearly distinguishable anymore. Lateral conchoidal fractures could also be identified (upper region of the photograph). At the highest force ($F = 1.839$ kN), the crack and fracture features just described were observed. In the range of the conchoidal fracture, fracture lances could be noted.

**Table 2** Indentation force effects on fracture morphology (see "Generalization of indentation force effects" section for detailed descriptions)

| Indentation force in kN | Image[a] | Comments |
|---|---|---|
| 0.153 | 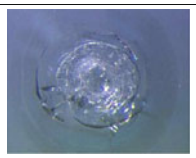 | Center not deformed<br>Ring with slight damages<br>Weak radial vent cracks<br>Outer ring crack |
| 0.307 | 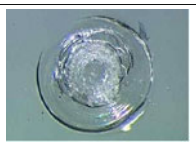 | Center not deformed<br>Ring with slight damages<br>Outer ring crack<br>Right: few fracture lances |
| 0.613 | 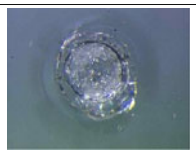 | Center not deformed<br>Ring of crushed material<br>Slight radial vent cracks<br>Bottom left: few fracture lances |
| 0.981 | 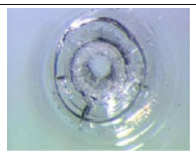 | Center not deformed<br>Ring of crushed material<br>Radial vent cracks<br>Lateral fractures<br>Outer ring crack |
| 1.226 | 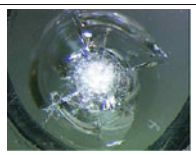 | Center heavily deformed<br>Radial vent cracks<br>Lateral conchoidal fractures<br>Outer ring crack<br>Bottom right: fragment |
| 1.471 | 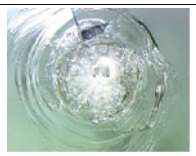 | Center heavily destroyed<br>Radial vent cracks<br>Lateral conchoidal fractures<br>Top: dislodged fragment |
| 1.839 | 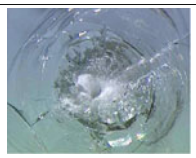 | Center heavily destroyed<br>Radial vent cracks<br>Lateral conchoidal fractures<br>Bottom: dislodges fragment<br>Lower section: fracture lances |

[a] Images are not to scale, but shown in different magnification levels in order to better illustrate details

## Fracture fragments in the inner ring section

At high forces ($F > 1.226$), the morphology of zone *1* as well as that of the inner ring *2* changed completely. Both regions were replaced by a zone in which the near-surface region was separated into segments by means of radial vent cracks. The appearance was comparable to that of a pie cut into pieces. The diameter of this zone, thus the length of the separated segments, depended on indentation force. Gorham et al. [8] have also reported the formation of such segments, and these authors could separate them from the glass surface. The general segment shape agreed

completely with the shape described above, and each segment was separated radially by means of a crack. This latter finding also agreed well with the observations in the present study. It suggests itself to interpret the radial separation cracks as the original boundary between (now destroyed) center and inner fracture band. Fractures of that kind could also be observed if the samples were indented with a diamond cone (120°). The fracture band *2* observed in this study may be comparable to a feature described in [7]. These authors reported about the formation of small debris which took place around the main Hertzian ring cracks. The generation of microscopically small fracture debris in the contact cross-section, observed at higher forces, can be attributed to compressive stresses acting in that region. This particular phenomenon is known from rock cutting investigations [31]. In that application, a layer of finely grained debris often leads to unwanted damping phenomena.

## Fracture lance formation

### Characteristics of fracture lance fronts

Fracture lance formation was observed in the curved sections of the lateral conchoidal fractures. The appearance of fracture lances in conchoidal shell-shaped fractures agreed with information provided in [17, 18, 26] for other testing situations. Examples for fracture lance fronts are provided in Fig. 6 for two force levels. It seemed that fracture lance fronts formed predominantly at the end of the conchoidal fractures, close to the free glass surface. Figure 7 provides a closer look at a fracture lance front. The discrete lances were very symmetrically arranged into the front, with equal orientation and discrete dimensions. More examples are provided in Figs. 8, 9, 10, 11, and 12. Again, the appearances of the lance fronts were symmetric, and the lances progressed parallel to each other in general. The very regular, systematic arrangement of individual lances into very distinguished fronts could be observed in all cases, and this was one of the most remarkable observations. Extensively branching "river lines" as described in [11, 32, 33] could not be identified.

Lance fronts appeared and disappeared with a certain periodicity, and their dimensions changed, in dependence of the particular local load situations. Figure 8 shows two lance fronts, $B$–$B'$ and $E$–$E'$, separated by a lance-free region, $C$–$C'$. The lance-free section was about 55 μm wide. Periodically occurring lance fronts have been reported in [34] as a result of the overlap of stresses from transversal ultrasound waves. The width of front $B$–$B'$ was much longer than that of $E$–$E'$. All individual lances were of equal length in the front $B$–$B'$; this was not the case in the front between $C$–$C'$ and $E$–$E'$. The spacing between individual lances increased if the indentation force increased. They varied between 28 μm ($F = 0.156$ kN) and 150 μm ($F = 1.839$ kN). These numbers are notably larger than numbers provided in [32] for brittle epoxy resins, where spacing of lances as small as 3 μm was reported. Widths and lengths of individual lances were also found to be dependent on the indentation force (see Fig. 13). At the highest force ($F = 1.839$ kN), the maximum length was about 700 μm, and the width was about 25 μm.

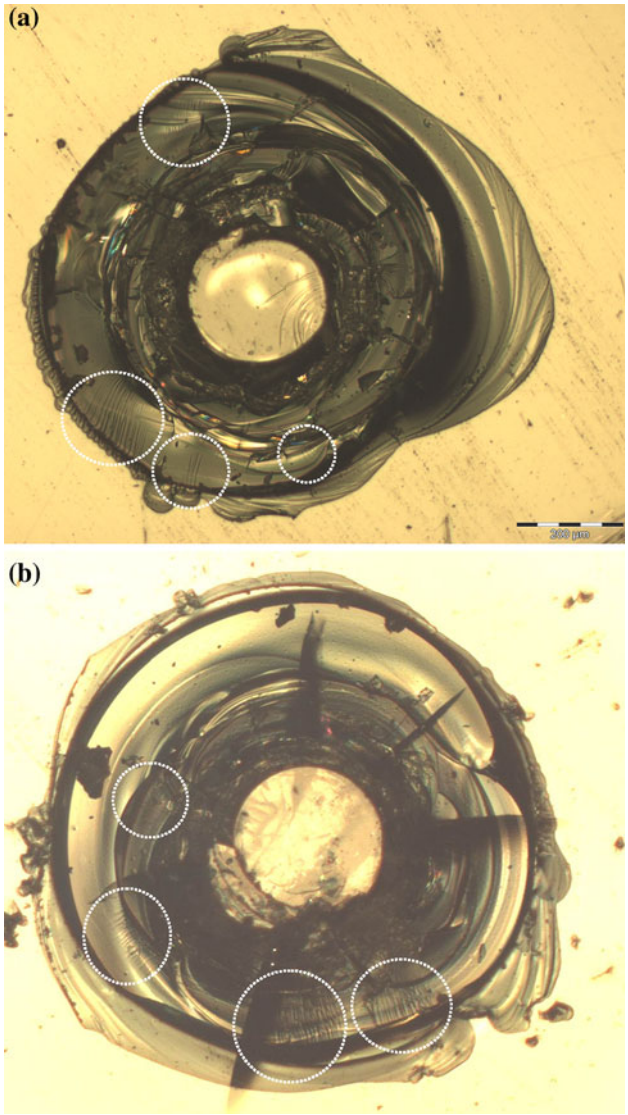


**Fig. 6** Conchoidal fracture with fracture lances (fracture lance fronts are marked). **a** $F = 0.153$ kN; scale: 200 μm. **b** $F = 0.307$ kN; image width: 1.6 mm

Of particular interest was the appearance of the lance fronts starting at $C$–$C'$ in Fig. 8. They were characterized by an exchange between long and short lances. A higher resolution revealed that the front $E$–$E'$ consisted of four sub-fronts.

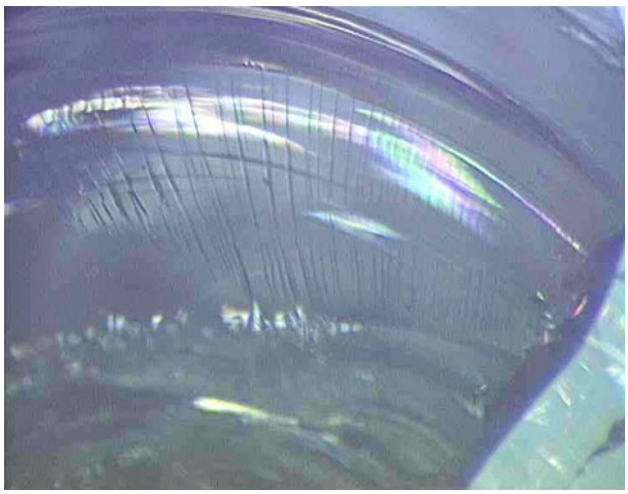

**Fig. 7** Formation of fracture lance fronts ($F = 1.839$ kN; image width: 3 mm)

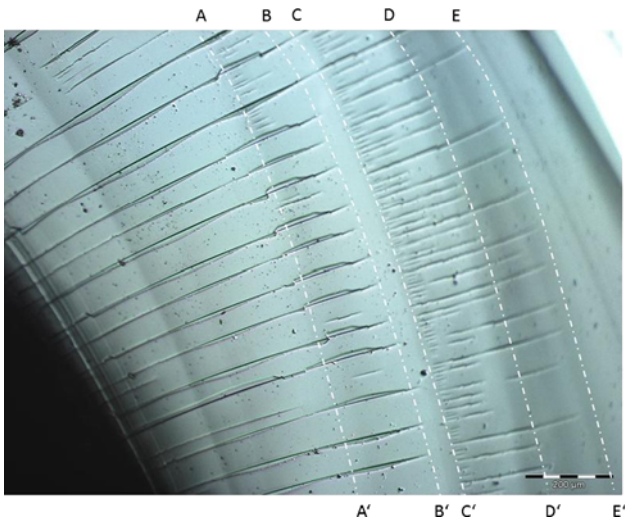


**Fig. 8** Formation of fracture lance fronts ($F = 1.839$ kN; scale: 200 μm)

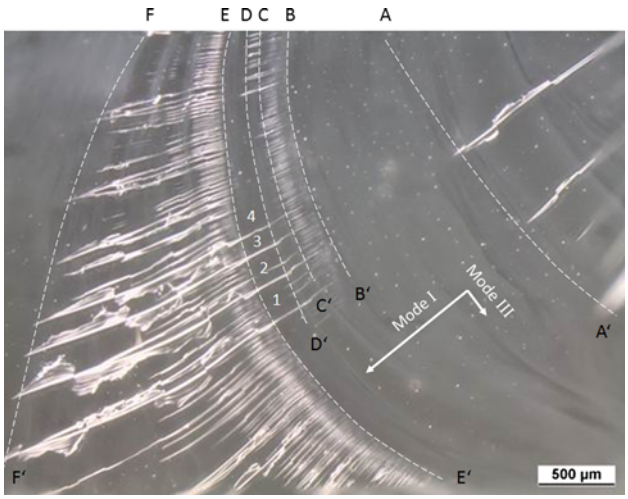


**Fig. 9** Formation of fracture lance fronts ($F = 0.981$ kN; scale: 500 μm)

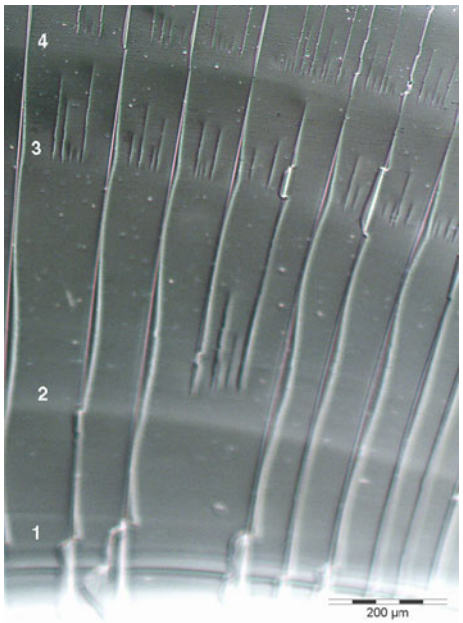


**Fig. 10** Formation of fracture lance fronts ($F = 1.839$ kN; scale: 200 μm; negative image)

However, "lance coarsening" in fracture propagation direction, as recently proposed in [35], could not be verified. The number of actively growing lances reduced with increase in lance lengths, whereas the lance lengths had always discrete numbers. The same observation could be made in Fig. 9 for the fronts $B$–$B'$ to $D$–$D'$, although the process did not occur as regular as in Fig. 8.

Figure 11 provides examples for stepwise progressing fractures, situated in the conchoidally fractured section of samples loaded at high indentation forces. Fracture lance fronts could be recognised in either photograph. In Fig. 11a, four symmetric fracture fronts ($A$–$A'$ to $D$–$D'$) could be recognised. The lances run above and underneath the edges of the fracture steps. Their lengths were between 50 and 100 μm, independently on their location (whether at the horizontal or the vertical section of the step). Further right in the photograph, smaller steps could be recognised about whose edges lances could be identified, too. The same phenomenon is again illustrated in Fig. 11b for a higher indentation force. Symmetric lance fronts ($A$–$A'$ to $C$–$C'$) could be distinguished at several fracture steps. These steps proceeded from the upper right to the lower left (see arrow).

Fracture lance fronts could also be identified if the samples were indented with a cone (diamond cone, 120°; $F = 0.153$ kN). As shown in Fig. 12, lances occurred in the lateral shell-shaped fractures. Discrete lances run

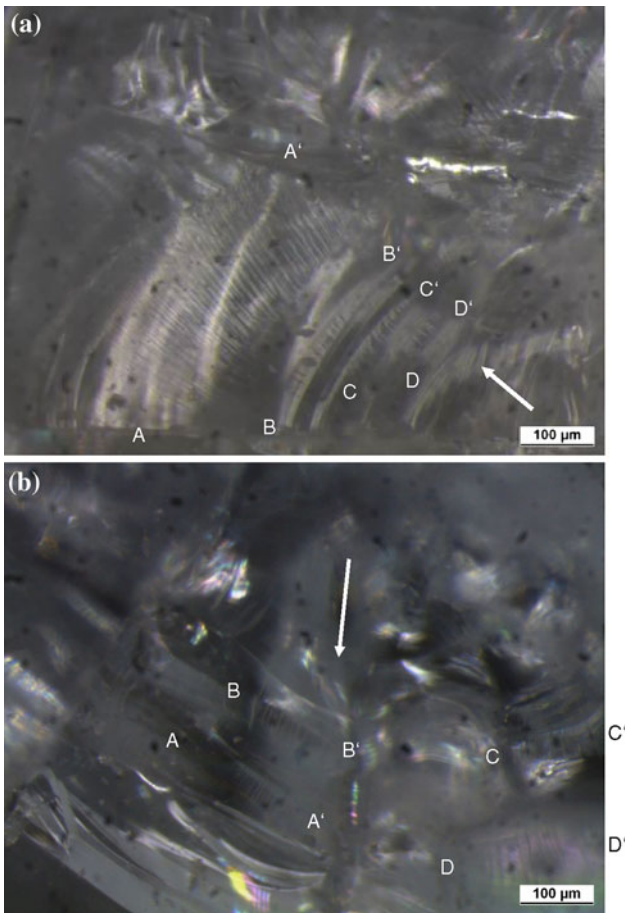


**Fig. 11** Fracture lance front formation on fracture steps (fracture propagation direction arrowed). **a** $F = 1.471$ kN; scale: 100 µm. **b** $F = 1.839$ kN; scale: 100 µm

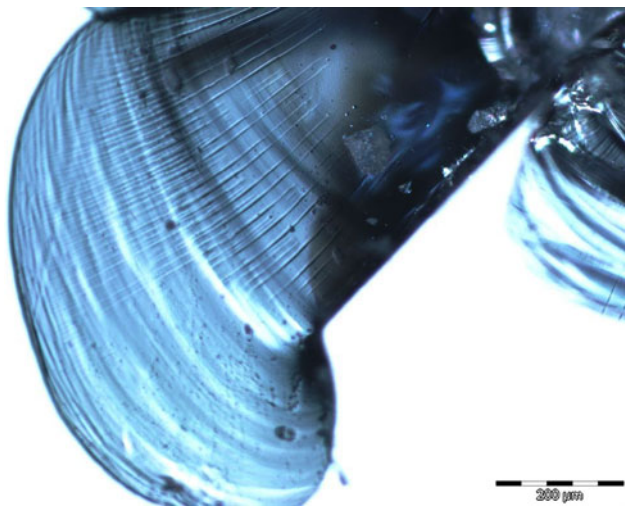

**Fig. 12** Fracture lance front formation on a lateral conchoidal fracture. Rockwell cone; cone angle: 120°; $F = 0.156$ kN; scale: 200 µm

parallel to each other in a very symmetric style. Their lengths were about 200 µm, and the distances between individual lances were about 20 µm; thus in the same order of magnitude as for the spherical indenter.

## Characteristics of discrete fracture lances

Although the lance fronts showed equal orientations, they differed from each other in terms of dimensions and structures. Fracture lance length histograms for different lance fronts are provided in Fig. 13 for two indentation force levels. Only discrete length numbers were detected. The numbers of lances are provided for a front length of 1.0 mm. It is interesting to note that the lower indentation force led to the formation of longer lances in general. A cumulative lance length distribution is provided in Fig. 14.

Figure 15 shows photographs of fracture lances taken under polarized light. It can be recognized that the geometries of the lances were independent of the lance sizes. The very large fracture lance in Fig. 15a and the much smaller fracture lances in Fig. 15b owned identical structures, even in details. This result can be interpreted as an element of self-similarity.

Another notable feature, also illustrated in Figs. 8 and 9, was that individual lances changed radial orientation. Remarkable examples for this particular behavior could be recognized in front $A$–$A'$ in Fig. 8, which was the first front in fracture propagation direction: over a distance of about 150 µm, the lances changed orientation from right to left (seen in fracture propagation direction). Other examples can be found in Fig. 9 in the crack fronts $A$–$A'$ and $F$–$F'$: the very pronounced lances changed orientation from right to left (seen in fracture propagation direction). This observation was of particular interest because $A$–$A'$ was the first front and $F$–$F'$ was the last front, in fracture propagation direction. Figure 16 illustrates extreme fracture plane response: the lance at the very left and the lance in the center of the photograph changed radial orientations seven times over a distance of about 45 µm.

A notable feature, illustrated in Fig. 9, was that some very long lances (lengths of about 2,000 µm), starting from $B$–$B'$ and designated *1* to *4*, crossed the lance-free region and integrated into the fronts $E$–$E'$ to $F$–$F'$. The phenomenon could also be recognized in Fig. 10 for a higher indentation force. At these very long lances, the tilted fracture planes were partly frayed in Fig. 9. The widths of the frayed areas were up to 120 µm. [This special feature is very well clarified in comparison with Fig. 8 (front $A$–$A'$).] A very similar image is provided in [9].

A distinct phenomenon, apparent in Figs. 8 and 10, was the appearance of distinguished horizontal gray bands at particular sections of the fracture surfaces. These bands are marked *1* to *4* in Fig. 10. It can be seen that the location of

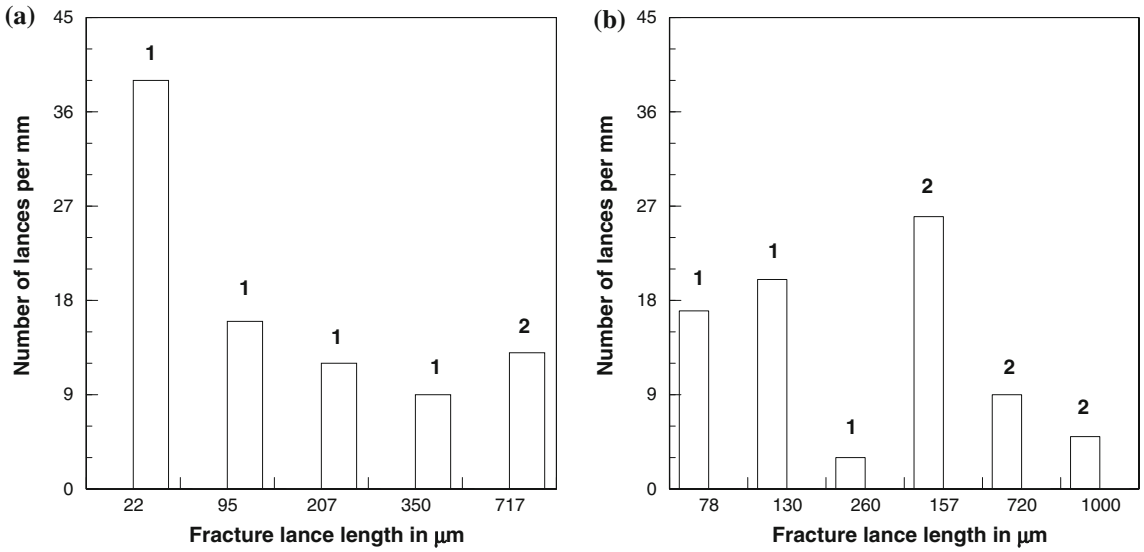


**Fig. 13** **a** Fracture lance length frequency for the fronts shown in Fig. 8 ($F = 1.839$ kN). *1* Lance front $C$–$C'$ to $E$–$E'$; *2* lance front from 0 to $B$–$B'$. **b** Fracture lance length frequency for the fronts shown in Fig. 9 ($F = 0.981$ kN). *1* Lance front $B$–$B'$ to $D$–$D'$; *2* lance front from $E$–$E'$ to $F$–$F'$

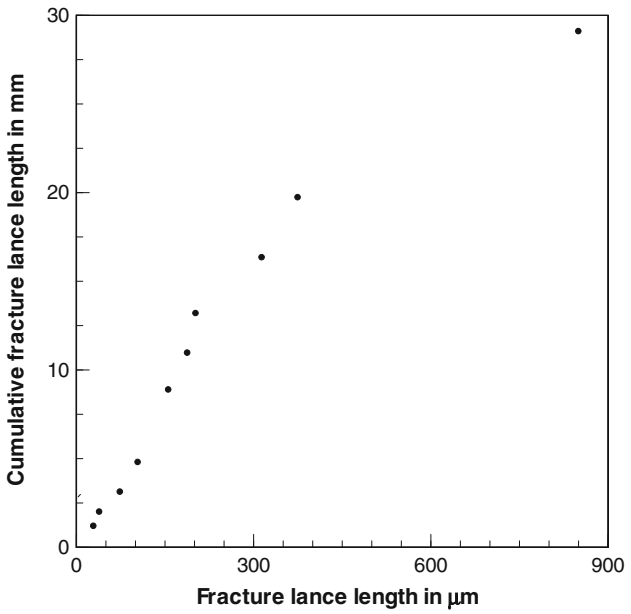


**Fig. 14** Cumulative fracture lance length distribution for $F = 0.981$–$1.839$ kN

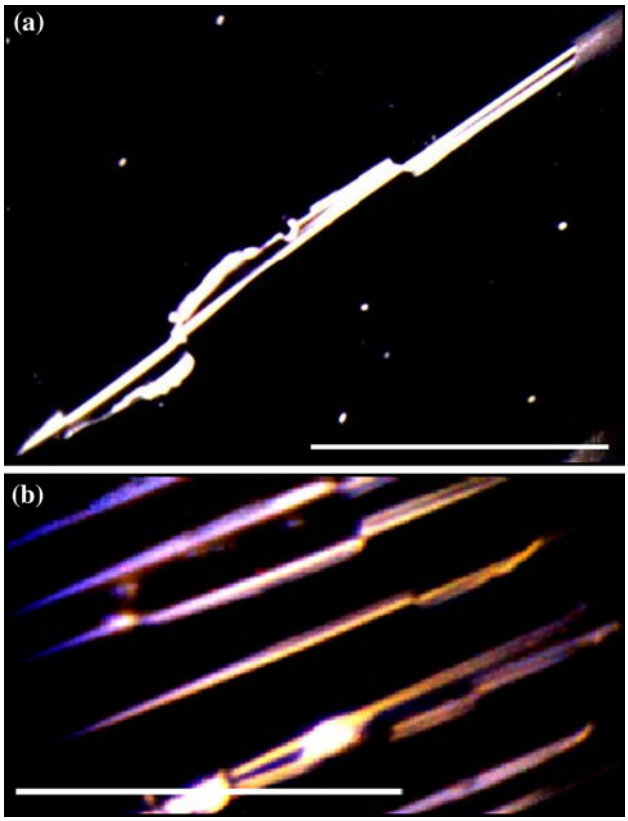


**Fig. 15** Self-similarity of fracture lances (photographs taken with polarized light). **a** Fracture lance from lance front $A$–$A'$ in Fig. 9; scale: 500 μm. **b** Fracture lances from lance front $C$–$C'$ in Fig. 9; scale: 100 μm

these bands corresponded with distinct features of lance formation. Changes in radial lance orientation at already existing discrete lances could be observed as well as the formation of new periodic lance fronts.

Another phenomenon, illustrated in Fig. 17, was the coalescence of fracture marks into crack growth direction or lance coarsening. Two lances met typically under an angle of about 20° in crack growth direction, and the distances between the newly formed tips were between 40 and 100 μm. This phenomenon was probably first described in [16]. The phenomenon, and especially the fact that lances branch against the crack grow direction, was also identified in [11] during indentation tests on brittle resin.

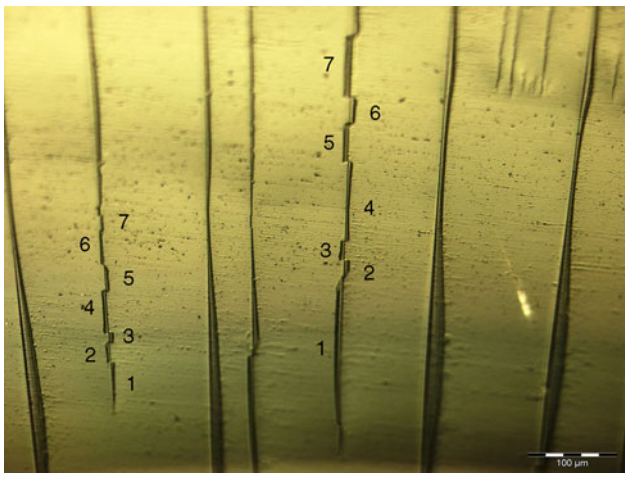


**Fig. 16** Conchoidal fracture with fracture lances, numbers *1–7* illustrate changes in radial direction ($F = 1.839$ kN; scale: 100 µm). Fracture propagation direction from bottom to top

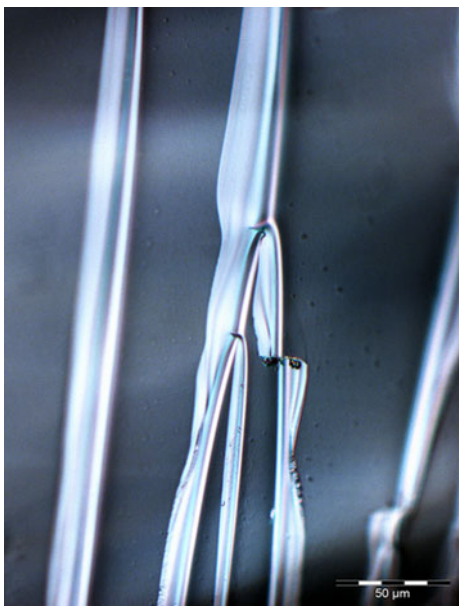


**Fig. 17** Fracture lance coalescence ($F = 1.839$ kN; scale: 50 µm)

The three-dimensional structure of converging fracture lances is very well illustrated in Fig. 17. Based on that particular image, the step height of the tilted crack front section can be approximated to be about 10 µm.

## Discussion of fracture morphology

### General fracture morphology

Under completely elastic contact between a spherical indenter and a plane sample, ring cracks form on the surface. This response is illustrated in the upper photographs of Table 2. At high indentation forces, double rings can form [3, 5]. A further increase in indentation force promotes the formation of cone cracks which progress into the sample under defined angles and which cannot be recognized on the surface. If indentation force increases further, other crack types form, while the precise mechanisms of crack, or fracture, formation depend on the glass composition. The glass utilized in this study was a glass with network formers, which is verified by EDX analysis (see Fig. 1). It is known that this glass type responds to local loading with plastic deformation; in contrast to pure silicate glasses which respond through structure densification [36, 37]. The identified lateral and radial vent cracks can, therefore, be explained with standard elastic-plastic indentation models [38]. During the loading period, if a critical indentation force is exceeded, shear stresses are generated which promote the formation of median vent cracks. In the unloading period, stress mismatch leads in particular to the formation of lateral vent cracks. They are produced by a tensile stress and often extend to the surface, resulting into chipping of the surface of the target as has been observed in this study (see Table 2). If these cracks reach the surface, they can be recognized as conchoidal fractures. A very similar appearance can be recognized if glass samples are cyclically (for example, after $10^4$ cycles) loaded with ball-shaped indenters [39]. The conchoidal fractures featured the fracture lances described in "Discussion of fracture lance formation" section. They are separated via near-surface radial vent cracks.

### Contact diameter, radial and lateral vent cracks

The relationship between contact diameter (in this article diameter of the center *1*; see Fig. 2) and indentation force can be described with Hertz's solution for elastic material response [38]:

$$\frac{D_1}{2} = \left(\frac{4 \cdot k \cdot F \cdot R_I}{3 \cdot E_T}\right)^{1/3}, \quad D_1 \propto F^{1/3} \tag{1}$$

In that equation, $D_1$ is the diameter of the center, $F$ is the indentation force, $R_I$ is the indenter radius, and $E_T$ is Young's modulus. The constant $k$ is the combined modulus of the indenter and the target. It depends on the elastic properties of the materials [38]:

$$k = \frac{9}{16} \cdot \frac{E_T}{E_I} \cdot [(1 - \nu_T^2) + (1 - \nu_I^2)] \tag{2}$$

In that equation, $E_T$ is Young's modulus and $\nu$ is the Poisson ratio. The subscript I stands for indenter material and the subscript $T$ stands for target material. For the material pairing used in this study, $k = 0.153$. The relationship $D_1 \propto F^{1/3}$, depicted through Eq. 1, is plotted in Fig. 3. Although a linear relationship (correlation = 0.94) could be

established between the two parameters, quantitative agreement could be noted for low and moderate contact forces only. The values of the contact diameters measured on the samples indented with high forces were notably larger than the values delivered by theory. In these cases, elastic-plastic material response mechanisms, which are not considered in Hertz' analysis, played a notable role, and the contact diameter could rather be interpreted as the diameter of elastically deformed material sections (see Table 2). In these cases (open symbols in Fig. 3), the measurements delivered a more distinct relationship: $D_1 \propto F^{8/5}$. This relationship assumes a much higher sensitivity of the center size to changes in indentation force. The onset of yield in indented materials can be approximated as follows [40]:

$$F_Y = K \cdot H_T \cdot \left(\frac{H_T}{E_T}\right)^2 \cdot R_I^2. \tag{3}$$

The dimensionless constant $K$ can be calculated as follows [38]:

$$K = \left(\frac{1.1 \cdot \pi}{c}\right)^3 \cdot \left(\frac{3 \cdot (1 - \nu_T^2)}{4}\right)^2. \tag{4}$$

The parameter $c$ is a constraint factor; for elastic-plastic solids: $c \cong 2$ [41]. The dimensionless constant is $K = 0.93$ for the soda-lime glass. For the material pairing used in this study, Eqs. 3 and 4 deliver a rather low value of $F_Y = 8.4$ N. This low yield onset depicts a sensitivity to elastic-plastic response, which may be one explanation for the deviations of the measured contact diameters in Fig. 3 from the theoretically estimated numbers. The low yield onset is partly due to the low hardness of the soda-lime glass, but mainly due to the small radius of the indenter used in this study. If a radius of $R_I = 2.5$ mm would be considered, as employed in [7], the yield onset would become as high as $F_Y = 210$ kN.

The relationship between indentation force and diameter of the outer ring (*4*, respectively *7*, see Fig. 2) is shown in Fig. 5. Based on microscopic inspections of the crack systems, it was assumed that the radius of the outer ring could be expressed through the length of the lateral vent cracks for the higher indentation forces (compare Fig. 2 and Table 2). The following relationship to the indentation force can be derived [42, 43]:

$$D_2 \approx L_L = \left\{\left(\frac{0.1}{9} \cdot \frac{\tan^2 \beta}{\sqrt{\pi \cdot k}}\right) \cdot \left[\frac{F^2}{E_T \cdot \Gamma_{Ic}} \cdot \left(\frac{F}{\sigma_Y}\right)^{1/2}\right]\right\}^{1/4}, \quad D_2 \propto F^{5/8}. \tag{5}$$

In that equation, $L_L$ is the length of lateral fractures, $F$ is the indentation force, $\beta$ is the indenter angle, $\Gamma_{Ic}$ is the mode-I toughness, and $\sigma_Y$ is the yield stress. The relationship $D_2 \propto F^{5/8}$ is plotted in Fig. 5. A linear relationship could be established for moderate and high indentation forces (correlation = 0.94). The outer ring diameters formed at the two low indentation forces (see open symbols in Fig. 5) could not be linked to Eq. 5, which was derived based on elastic-plastic material response. The results plotted in Fig. 5 do not verify results reported in [8]. These authors claimed a linear relationship between outside diameter and indentation force ($D_2 \propto F$). However, statistical parameters (correlation, standard deviation) were not provided by these authors. The regression line in Fig. 5 intersects the abscissa at $F^{5/8} = 0.1$, which corresponds to $F = 25$ N. This threshold indentation force for the introduction of lateral vent cracks is in good agreement with values reported in [4] for CaAlSi glass loaded with 1.0 mm tungsten carbide indenters. The relationship between radial vent crack length and indentation force was modeled in [30], who proposed the following relationship:

$$F \propto D_I \cdot L_R^{1/2} \tag{6}$$

In that equation, $D_I$ is the indenter diameter. The results plotted in Fig. 4 confirm this relationship. The correlation between experimental results and model was 0.93.The mean indentation pressure, $p_0$, can be calculated with the following equation [44]:

$$p_0 = \frac{4 \cdot F}{\pi \cdot D_I^2}. \tag{7}$$

The values estimated for the condition in this study were between 4 and 12 GPa, which notably exceed the compressive strength of soda-lime glass (which is typically at about 1 GPa).

## Discussion of fracture lance formation

### General considerations

The formation of fracture lances in glass was qualitatively described in the early works of [16–19]. Recent reviews are provided in [35, 45]. The general situation of lance fracture formation may be discussed based on Fig. 18. The lower section of the drawing provides the plane view of the fracture surface, while the upper section provides a cross-sectional view. According to a phenomenological hypothesis [17, 19], fracture lance formation occurs due to the local adjustment of the crack plane to changes in the direction of the maximum principle stress. In Fig. 18, the primary cleavage fracture, generated due to a tensile stress $\sigma_0$, propagates up to a point where the principal stress changes direction ($\sigma_1$) under an angle $\delta$. [In Fig. 9, this

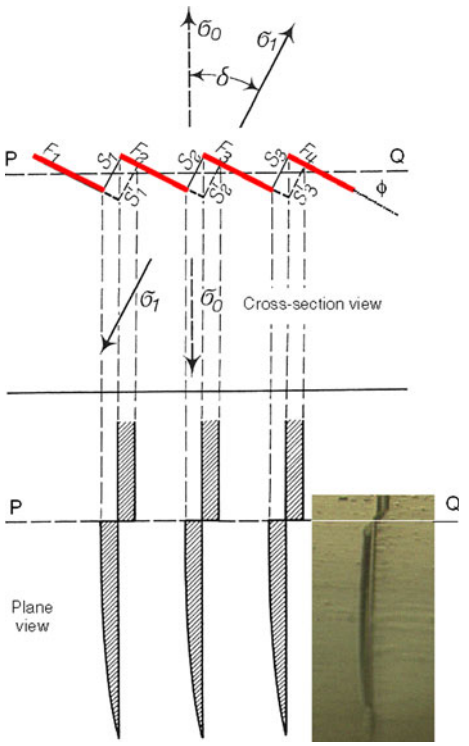


**Fig. 18** Formation of lancet fractures due to changes in the direction of the maximum principal stress from von $\sigma_0$ to $\sigma_1$ (adapted from [46]). The photograph in the lower right image section is added by the author

situation is illustrated through the arrowed mode I (tension) and mode III (shear).] This condition can be simulated experimentally by the superposition of a small amount of torsion [19] or due to ultrasound modulation [34]. This stress is still perpendicular to the direction of the primary fracture, but no longer perpendicular to the already formed fracture areas. A continuous adjustment of the crack plane along the entire crack front is not possible. Thus, the crack breaks into partial fronts, $F_1$ to $F_4$, which can adjust step-by-step to the new stress direction. The partial crack sections forming that front (inclined bold red lines) are designated *type A* cracks in [45]. They are inclined at an angle $\phi$ with respect to the nominal crack plane, but perpendicular to $\sigma_1$. The linking between the planes $F_1$ to $F_4$ can take place by different mechanisms. Lin et al. [45] categorized different linking modes. Among others, they distinguished a *hand shaking* mode, leading to a prismatic-shaped cross-section (which was probably first described in [16]; and in detail analyzed in [32]), and a *factory-roof* mode, leading to the cross-section $F_1$–$S_1$–$F_2$ provided in the upper section of Fig. 18 (see also [35]). The tilted planes can be linked to each other by either the lines $S_1$ to $S_4$ or the lines $S'_1$ to $S'_4$, and it happened (at the line $P$–$Q$) that the linking process jumps from one opportunity ($F_1$–$S_1$–$F_2$) to another ($F_1$–$S'_1$–$F_2$). This situation is highlighted by the dashed areas in the lower section of Fig. 18, and it can be recognised in Figs. 10 and 16. A detail from Fig. 16 is inserted into the lower right section of Fig. 18 in order to illustrate the agreement between schematic and real fracture lance appearance.

It is not completely clear what criterion rules the particular linking mode. Available models include the following: crack overlap model [47]; no-twist rule [32]; phase-field method [35]; and energy penalty criterion [45]. A detailed analysis of the lance formation process is beyond the scope of this article. The reader may refer to [35, 45] for detailed information.

## Phenomenological fracture lance front formation hypotheses

From the qualitative discussion, it can be concluded that a local change in the direction of the principal stress is the origin of fracture lance formation. This change can be caused by a targeted stress superposition or due to a stress-carrying disturbance in the material. Because fracture lances showed always up in a periodically occurring front-like mode, some type of a symmetric disturbance front could be assumed to be responsible for the change in the principal stress direction. Inspections of the fracture surfaces revealed indeed such fronts. Examples are provided in Fig. 10, where four distinguished smeared dark bands (*1–4*) can be recognised. If the lance fronts crossed a band, its appearance was notably affected. Either the radial orientations of the discrete lances changed or the formation of periodic lance fronts was introduced. It can be assumed that the gray horizontal bands express areas of locally modified densities which affected the reflectivity of the glass surface [48, 49]. Origins of density changes can be stress-redistributions (for example, due to pre-stressing or the built-up of hydrostatic pressure) or periodically traversing stress fronts. The local internal stress may superpose the principal (tensile) stress, introducing the above-mentioned mechanisms. The symmetric appearance of periodic lance fronts points to a particular ordering scheme for local stress modifications. The change in lance arrangement with fracture progression is a sign of changing lance formation conditions with crack length. A condition could be the gradual change in a rather low superimposed shear stress gradient [34]. Systematic experimental work is required to further explore this supposed effect.

Another observation worth to discuss is the fact that fracture lances were almost solely detected in the shell-shaped sections of the lateral fractures. This observation agreed with observations made in [15, 17, 18, 26] for other testing situations. As can be seen in Fig. 12, this observation was also made after the indentation of the glass with a sharp indenter. A conchoidal fracture is the summation of

many small interacting shells. The interaction of the shells can occur in the form of steps as illustrated in Fig. 11. These steps very often featured fracture lance fronts (see also [21]). A phenomenological model introduced in [18] can be applied in order to discuss this particular effect. Assuming that each individual shell has an individual starting point for fracture, and these points (notches) are close together, the fractures will not form individual fracture planes, but will merge. The formation of individual shells consumes part of the energy available for fracture propagation. The individual notches may have distinct orientations, and the fracture follows this orientation during the very early stage of fracture propagation. This orientation must not match the fracture plane to be formed. If enough energy is available, the fracture will quickly adjust. If an energy criterion is applied, it may be shown that, if several individual shells have formed, not enough energy is left for the fracture front to immediately adjust. It will rather follow the original orientation. Theoretical and experimental work is required to further explore the detailed stress situations in the final section of the radial shell-shaped fractures in indented brittle materials.

## Elements of fractal geometry

It is known that glass fracture surfaces can show a fractal character [22, 50]. Elements of fractal geometry have been applied to fracture lance propagation, in particular to the interpretation of "river lines," in [33]. It has been shown already in Fig. 15 that the particular geometry of an individual lance was independent of its length. This indicates that some ordering principle may be involved in the lance formation, and that the lances may exhibit some aspects of self-similarity or self-affinity. A further fractal characteristic is illustrated in Fig. 19 in connection with the formation of periodic lance fronts. The spacing between discrete lances is reduced in a defined rhythm if the lance front progresses. The original spacing, level $L_1$, is the spacing between the longest lances in the front. At the next step, two copies of that spacing are formed: $L_{1-1}$ and $L_{1-2}$. This process is repeated at the next step, $L_2$. The widths of the newly formed interspaces equates to about one-third of the width of the original interspace; for example: $L_{1-1} = L_{1-2} = 1/3L_1$. Figures 19b–d display typical examples. This structure is known from deterministic fractals, particularly from Cantor sets [51]. The structure of a typical triadic Cantor set is provided in Fig. 19a. The fractal dimension can be calculated as follows:

$$D_F = \frac{\ln N}{\ln r}. \tag{8}$$

In that equation, $N$ is the number of copies formed at each step and $n$ is the reduction factor. For the conditions illustrated in Fig. 19, the following case applies:

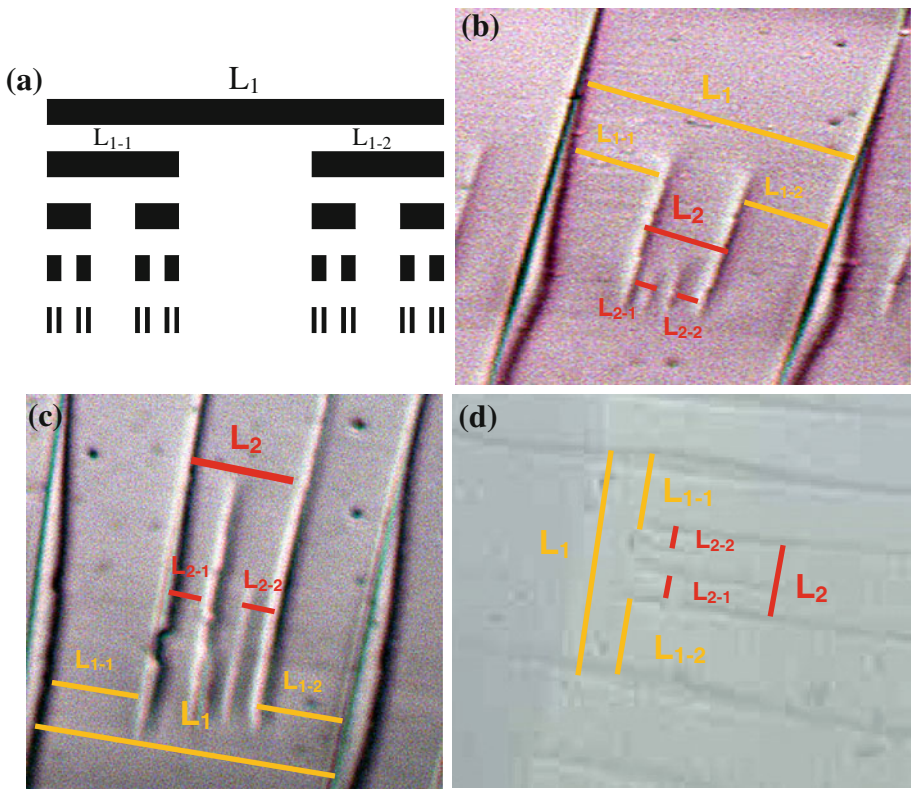


**Fig. 19** Fractal characteristics of lance front formation (see also Figs. 8, 10, 12). **a** Triadic Cantor set with the fractal dimension: ln 3/ln 2 = 0.63 (adapted from [51]). **b–d** Examples from three fracture lance fronts

$D_F = \ln 2/\ln 3 = 0.63$. Therefore, the process is characterized by a fractal dimension. It can be seen in Fig. 12 that this fractal feature also appeared during the indentation with a cone. It can therefore be considered a general phenomenon of indentation processes in glasses. Whether or not the fractal approach is of value in describing the process of fracture lance formation remains to be demonstrated through further research, but it provides arguments for a geometric ordering principle behind the process.

## Summary and conclusions

During the indentation of a thick glass plate with a spherical indenter, a variety of complex fracture figures developed. A systematisation of these figures showed a basic structure, consisting of four individual zones. The detailed characteristics of these zones depended on indentation force.

The appearance of fracture lances was found to be a definite part of indentation fracture surfaces. The following relationships could be found:

- Lances formed during the transition of conchoidal (lateral) fractures and their formations were bound to the elastic-plastic period of the indentation process.
- Lances formed always in a front-type mode. Lance fronts were characterized through a high degree of symmetry.
- Periodical lance fronts formed under particular stress conditions.
- Particular features of lance fronts seemed to be related to changes in optical properties at particular surface sections.
- Lance lengths had discrete numbers.
- Lances tended to change radial directions under certain stress conditions.
- Individual lances merged in crack propagation direction.
- Lance geometries were self-similar.
- Many lance fronts showed features of Cantor sets.

Although the detected lance formation characteristics help to better understand the fracture processes in glass during the elastic-plastic loading period, systematic research and theoretical work are required to utilize the fracture lance formation processes for material design optimization.

**Acknowledgement** This investigation was supported by the German Research Association (DFG), Bonn, Germany. The working group "Endogene Dynamik" of the Faculty Georesources and Materials Technology at the RWTH Aachen has kindly permitted the use of its high-performance optical microscopes.

## References

1. Buehler MJ, Xu Z (2010) Nature 464(4):42
2. Auerbach F (1891) Ann Phys Chem XLIII:61
3. Peter K (1964) Glastechn Ber 37(7):333
4. Swain MV, Hagan JT (1976) J Phys D 9:2201
5. Persson J, Breder K, Rowcloffe DJ (1993) J Mater Sci 28:6484. doi:10.1007/BF01352218
6. Salman AD, Gorham DA (1997) J Mater Sci Lett 16:1099
7. Gorham DA, Salman AD (1999) Wear 233–235:151
8. Gorham DA, Salman AD, Tan H (2002) Philos Mag A 82(10): 2231
9. Quinn GD (2007) Fractography of ceramics and glasses. NIST Special Publication 960-16. NIST, Gaithersburg, MD
10. Smekal AG (1937) Glastechn Ber 15(7):259
11. Hull D (1996) J Mater Sci Lett 15:651
12. Kirchner HP, Gruver RM (1977) In: Taplin DM (ed) Proceedings of 4th international conference on fracture, vol 3. Pergamon Press, New York, pp 959–965
13. Marshall DB, Lawn BR, Mecholsky JJ (1980) J Am Ceram Soc 63(5–6):358
14. Hockey BJ, Lawn BR (1975) J Mater Sci 10:1275. doi:10.1007/BF00540816
15. Tandon R, Buchheit TE (2007) J Am Ceram Soc 90(2):502
16. Murgatroyd JB (1942) J Soc Glass Technol 26:155
17. Smekal AG (1953) Österr Ingenieur Archiv VII:49
18. Kienle R (1960) Glastechn Ber 33(9):321
19. Sommer E (1969) Eng Fract Mech 1:539
20. Yoda M (1990) J Am Ceram Soc 73(7):2124
21. Espinosa HC, Xu Y (1997) J Am Ceram Soc 80(8):2061
22. Chai H, Ravichandran G (2009) Int J Impact Eng 36(3):375
23. Kulawansa DM, Jensen LC, Langford SC, Dickinson JT (1994) J Mater Res 9(2):476
24. Kocanda S, Kuzmenko A, Pismennyi NN, Sadovskii Y (1986) Strength Mater 18(9):1160
25. Frid V, Bahat D, Rabinovich A (2005) J Struct Geol 27:145
26. Wiederhorn SM, Hockey BJ (1983) J Mater Sci 18:766. doi:10.1007/BF00745575
27. Wereszczak AA, Johanns KE, Kirkland TP, Anderson CE, Behner T, Patel P, Tempelton DW (2006) Report ADM002075. Oak Ridge National Laboratory, Oak Ridge, TN, 01 November 2006
28. Maekawa I, Shin H, Miyata H (1991) Eng Fract Mech 40(4):869
29. Satapathy S (2001) Int J Solids Struct 38:5833
30. Kirchner HP, Ragosta JA (1983) J Am Ceram Soc 66(4):293
31. Kuo SQ, Liu HY, Lindqvist PA, Tang CA (2004) In: Proceedings of Sinorock Symposium, Three Gorges Dam Site, China, 18–21 May, 2004
32. Hull D (1995) Int J Fract 70:59
33. Djordjevic ZV, Li X, Shin WS, Wunder SL, Baran GR (1995) J Mater Sci 30:2968. doi:10.1007/BF00349671
34. Kerkhof F (1970) Bruchvorgänge in Gläsern. Verlag der deutschen Glastechnischen Gesellschaft, Frankfurt am Main
35. Pons AJ, Karma A (2010) Nature 464(4):85
36. Arora A, Marshall DB, Lawn BR (1979) J Non-Cryst Sol 31:415
37. Peter K (1970) J Non-Cryst Sol 5:103
38. Fischer-Cripps AC (2007) Introduction to contact mechanics, 2nd edn. Springer, Heidelberg
39. Kim DK, Jung YG, Peterson IM, Lawn BR (1999) Acta Mater 47(18):4711
40. Rhee YW, Kim HW, Deng Y, Lawn BR (2001) J Am Ceram Soc 84(3):561
41. Bushby AJ, Swain MV (1995) In: Bradt RC et al (eds) Plastic deformation of ceramics. Plenum Press, New York, pp 161–172
42. Marshall DB, Lawn BR, Evans AG (1982) J Am Ceram Soc 65(11):561

43. Chen X, Hutchinson JW, Evans AG (2005) J Am Ceram Soc 88(5):1233
44. Lawn BR (1998) J Am Ceram Soc 81(8):1977
45. Lin B, Maer ME, Ravi-Chandar K (2010) Int J Fract 165(2):175
46. Kerkhoff F (1975) Glastechn Ber 48(6):112
47. Swain MV, Lawn BR, Burns SJ (1974) J Mater Sci 9:175. doi: 10.1007/BF00550939
48. Gardon R (1978) J Am Ceram Soc 61(3):143
49. Ji H, Keryvin V, Rouxel T, Hammouda T (2006) Scripta Mater 55:1159
50. Russ JC (1994) Fractal surfaces. Plenum Press, New York
51. Mandelbrot B (1987) Die fraktale Geometrie der Natur. Birkhäuser Verlag, Basel